ELSEVIER

International Journal of Heat and Fluid Flow 23 (2002) 601–614

International Journal of HEAT AND FLUID FLOW

www.elsevier.com/locate/ijhff

Large eddy simulation of the turbulent flow past a backward-facing step with heat transfer and property variations

Ravikanth V.R. Avancha, Richard H. Pletcher *

Department of Mechanical Engineering, Iowa State University, Ames, IA 50011, USA

Abstract

The heat transfer and fluid mechanics of a turbulent separating and reattaching flow past a backward-facing step are studied using large eddy simulation. A fully coupled, collocated-grid, low-Mach number preconditioned, compressible formulation employing central differences was developed to conduct the simulations. A sixth order compact filter was used to prevent pressure–velocity decoupling. A dynamic sub-grid scale procedure employing the compressible version of the Smagorinsky model has been used to capture the effects of the small scales. The isothermal turbulent flow past the step, at a Reynolds number of 5540 (based on the step height and upstream centerline velocity) and a Mach number of 0.006, was simulated to validate the formulation. Subsequently, the bottom wall downstream of the step was supplied with a uniform wall heat flux; three simulations with increasing heat flux levels were conducted. The viscous sub-layer played a critical role in controlling the heat transfer rate. Streamwise and wall-normal turbulent heat fluxes were of the same order of magnitude. The Reynolds analogy did not hold in the recirculation region. However, the Stanton number profiles showed a striking similarity with the fluctuating skin-friction profiles.

Keywords: Large eddy simulation; Backward-facing step; Turbulent flow; Flow separation; Heat transfer; Variable property; Finite volume; Collocated grid

1. Introduction

Turbulent flows with separation and reattachment, involving heat transfer, occur commonly in critical components of many engineering systems like gas turbine engines, heat exchangers, combustors, and electronic equipment. Large variations of the local heat transfer coefficients as well as augmentation of overall heat transfer are caused by these flows. Conventional turbulence modeling methods, such as the Reynolds averaged Navier–Stokes (RANS) approach, have proved to be generally inadequate in predicting the effects of turbulent separating and reattaching flows with heat transfer. The description of turbulent flows using the large eddy simulation (LES) method is an active area of research and the simulation of complex turbulent flows, such as those involving separation and reattachment in the presence of heat transfer, is essential in the development of the method as a tool to predict flows of engineering interest. Large eddy and direct numerical simulations, owing to the use of little or no ad hoc modeling, can reveal aspects of the fundamental physics of such flows and provide details that cannot be measured easily by experiments. Models used in RANS approaches can then be refined based on information obtained from such simulations.

Within the framework of a fairly simple geometry, the turbulent flow past a backward-facing step, involving significant heat transfer, consists of distinctly different complex flow regimes that include flow separation, reversal and recovery in the presence of a strong adverse pressure gradient, mixing, reattachment, and redeveloping velocity and thermal boundary layers. This geometry is an excellent choice for a study of the characteristics of flow separation and reattachment.

RANS approaches using standard turbulence models have not been successful in predicting all the flow features and heat transport mechanisms for this geometry. Abrous and Emery (1996) reviewed the submissions to benchmark study and reported that only the results for the streamwise velocity and dissipation were in agreement amongst all contributors. Substantial differences in the turbulent kinetic energy, skin-friction and

* Corresponding author.
E-mail address: pletcher@iastate.edu (R.H. Pletcher).

0142-727X/02/$ - see front matter
PII: S0142-727X(02)00156-X

Nomenclature

c	local speed of sound
C_f	coefficient of skin friction $(= 2/Re)[(\mu/\rho)\,\partial u/\partial y]_{\mathrm{w}})$
C_p	specific heat at constant pressure
C_{s}	Smagorinsky sub-grid-scale (SGS) model coefficient
C_v	specific heat at constant volume
h	step height or heat transfer coefficient $(= q_{\mathrm{w}}/(T_{\mathrm{wall}} - T_{\mathrm{bulk}}))$
k	thermal conductivity
$\mathscr{L}$	amplitude variation of characteristic wave
L	characteristic size of the domain
L_{ref}	reference length
M	maximum Mach number in the flow
M_{ref}	reference Mach number
Nu	Nusselt number $(= hL_{\mathrm{ref}}/k_{\mathrm{bulk}})$
Pr	Prandtl number $(= \mu C_p/k)$
Pr_{T}	turbulent Prandtl number
p	thermodynamic pressure
Q_j	SGS turbulent heat flux vector
Q_{w}	normalized wall heat flux $(= q^*_{\mathrm{w}}/\rho_{\mathrm{ref}}U_{\mathrm{ref}} \times C_p T_{\mathrm{ref}})$
q^*_{w}	dimensional wall heat flux
q_{w}	normalized wall heat flux (alternate normalization) $(= q^*_{\mathrm{w}}/[k_{\mathrm{ref}}T_{\mathrm{ref}}/L_{\mathrm{ref}}])$
q_j	heat flux vector
R	gas constant
Re	Reynolds number $(= \rho_{\mathrm{ref}}U_{\mathrm{ref}}L_{\mathrm{ref}}/\mu_{\mathrm{ref}})$
S_{ij}	strain rate tensor
St	Stanton number $(= Nu/RePr = h/\rho_{\mathrm{ref}}U_{\mathrm{ref}}C_p)$
T	thermodynamic temperature
T_{bulk}	bulk temperature
T_τ	friction temperature $(= q_{\mathrm{w}}/\rho_{\mathrm{w}}C_p u_\tau)$
T_{wall}	wall temperature
u_τ	friction velocity $(= [\tau_{\mathrm{w}}/\rho_{\mathrm{w}}]^{1/2})$
u^*_τ	semi-local friction velocity $(= [\tau_{\mathrm{w}}/\rho(y)]^{1/2})$
u, v, w	cartesian non-dimensional velocity components in x, y, z directions
u_i	velocity vector, $i = 1, 2, 3$
u^+	velocity in wall coordinates $(= u/u_\tau)$
u^*	velocity in semi-local coordinates $(= u/u^*_\tau)$
x, y, z	cartesian coordinates
y^+	distance to wall in wall coordinates $(= \delta_y u_\tau/\nu_{\mathrm{w}})$
y^*	distance to wall in semi-local coordinates $(= \delta_y u^*_\tau/\nu(y))$
x_{r}	mean reattachment length

Greeks

α_{T}	eddy diffusivity
γ	ratio of specific heats
Δ	grid filter width
$\hat{\Delta}$	test filter width
δ	Kronecker delta
δ_y	distance to closest wall
μ	molecular dynamic viscosity
μ_{T}	SGS turbulent viscosity
ν	molecular kinematic viscosity $(= \mu/\rho)$
ν_{T}	SGS turbulent kinematic viscosity $(= \mu_{\mathrm{T}}/\rho)$
ρ	thermodynamic density
σ	a constant used in Eq. (12)
$\sigma_{i,j}$	shear stress tensor
τ_{w}	wall shear stress
τ_{ij}	SGS stress tensor
ϕ	a generic variable

Subscripts

av	average
bulk	bulk property
i, j, k	indices for cartesian coordinates
ref	reference quantity
rms	root mean square
w, wall	wall value
x, y, z	associated with cartesian direction

Superscripts and other symbols

$*$	dimensional variable or semi-local coordinates
$+$	wall coordinates
$'$	fluctuation with respect to ensemble average
$''$	fluctuation with respect to Favre ensemble average
$-$	resolved or large scale component of filtered quantity
$\sim$	resolved or large scale component of Favre filtered quantity
$\langle\ \rangle$	ensemble averaged quantity
$\langle\ \rangle_{zt}$	ensemble averaged in spanwise (z) direction and in time

wall-normal velocity profiles were reported. The Nusselt number predictions showed the greatest differences, and there did not appear to be any consistency in the computed points of maximum Nusselt number and the reattachment point. This was attributed to the marked differences in the computed wall temperatures. None of the methods were successful in producing a shape similar to the experiments of Mori et al. (1986) or those of Vogel and Eaton (1984).

Flow- and thermal-field calculations using a RANS approach with *modified* k–ϵ model were conducted by Abe et al. (1994, 1995) and the computed reattachment lengths and Stanton numbers were reported to be in agreement with the experimental data of Vogel and

Eaton (1984). Nagano and Shimada (1996) developed low-Reynolds-number type k–ϵ and k_t–ϵ_t (where k_t is the intensity of fluctuating temperature and ϵ_t is its dissipation rate) models that were constructed with the aid of DNS databases. The predicted mean temperature and turbulent heat flux showed the same tendency as the corresponding measurement, and the Stanton number distribution at a Prandtl number of 0.71 was reported to be in good qualitative and quantitative agreement with the data of Vogel and Eaton (1984). Ciofalo and Collins (1989) noted that the use of conventional wall functions with a constant non-dimensional thickness of the viscous sub-layer resulted in under-prediction of the heat transfer rates near and downstream of the reattachment point of separated shear layers. Therefore, they proposed an approach that allowed the non-dimensional thickness of the viscous sub-layer to vary as a function of the local turbulence intensity and reported better agreement with experimental heat transfer data for single backsteps and double symmetric expansions. However, a need for improvement in the heat transfer predictions upstream of reattachment was also suggested, since most wall function approaches fail to resolve the counter-rotating corner eddy.

LES, owing to the use of limited modeling, is a very attractive approach for the investigation into the thermal and flow physics of the turbulent separating and reattaching flow past a backward-facing step. Few RANS studies have considered property variations or density variations, both of which occur routinely when high levels of heat fluxes are involved. Also, most of the large eddy simulations to date have been carried out using staggered grid schemes. It is important to assess the performance of collocated grid methods for LES since staggered grid schemes can pose difficulties in the generalization to complex geometries (Zang et al., 1994, 1991; Rosenfeld et al., 1991; Shyy and Vu, 1991; Meakin and Street, 1988). Keeping in view the aforementioned issues, a low-Mach number preconditioned, compressible formulation of the NS equations on a collocated grid utilizing central differences has been employed to conduct the simulations.

To the best of the authors' knowledge no prior large eddy simulations have been reported for the turbulent flow past a backward-facing step with heat transfer. To date all the large eddy simulations were carried out to study the isothermal turbulent flow for this geometry (Akselvoll and Moin, 1995; Friedrich and Arnal, 1990; Arnal and Friedrich, 1991, 1992; Morinishi and Kobayashi, 1990; Neto et al., 1993).

2. Mathematical formulation

Turbulent flows are inherently three dimensional in nature, and possess a continuous spectrum of time and length scales that need to be captured accurately to understand the important flow characteristics. For any turbulent flow, the largest significant length scales are related to the domain size, and the small scales are related to the dissipative eddies where the viscous effects become predominant. LES is a method where the three-dimensional and unsteady motion of the large eddies is computed explicitly, and the non-linear interactions with the smaller eddies, which are assumed to be isotropic and universal, are modeled. In order to conduct large eddy simulations, a filtering procedure is applied to the NS equations that serves the purpose of defining the scales that would be resolved and the scales that would be modeled. For finite volume schemes, the finite grid resolution is an implicit top hat filter and achieves the objective of separation of resolvable and modeled scales. A density-weighted filtering (also referred to as Favre-filtering) is applied to the compressible formulations of the NS equations. For a quantity ϕ, the Favre filtered quantity $\tilde{\phi}$ is defined as $\overline{\rho\phi}/\bar{\rho}$.

2.1. Governing equations

In order to obtain the governing equations in their non-dimensional form, the solution variables are non-dimensionalized as

$$x_i = x_i^*/L_{\text{ref}} \quad u_i = u_i^*/U_{\text{ref}} \quad t = t^*/(L_{\text{ref}}/U_{\text{ref}})$$
$$\rho = \rho^*/\rho_{\text{ref}} \quad p = p^*/\rho_{\text{ref}}U_{\text{ref}}^2 \quad T = T^*/T_{\text{ref}}$$
$$\mu = \mu^*/\mu_{\text{ref}} \quad k = k^*/k_{\text{ref}} \quad R = R^*/(U_{\text{ref}}^2/T_{\text{ref}}) = 1/\gamma M_{\text{ref}}^2$$

where the reference quantities L_{ref}, U_{ref}, and T_{ref} are taken as the step height, upstream centerline velocity, and upstream temperature, respectively. Reference values of the density, dynamic viscosity and thermal conductivity are obtained at the reference temperature of 293 K. The non-dimensional, Favre-filtered compressible NS equations, neglecting the effects of buoyancy, pressure work, and viscous dissipation, are given as

$$\frac{\partial\bar{\rho}}{\partial t} + \frac{\partial\bar{\rho}\tilde{u}_j}{\partial x_j} = 0 \tag{1}$$

$$\frac{\partial\bar{\rho}\tilde{u}_i}{\partial t} + \frac{\partial\bar{\rho}\tilde{u}_i\tilde{u}_j}{\partial x_j} = -\frac{\partial\bar{p}}{\partial x_i} + \frac{\partial\bar{\sigma}_{ij}}{\partial x_j} - \frac{\partial\tau_{ij}}{\partial x_j} \tag{2}$$

$$\frac{\partial}{\partial t}(\bar{\rho}\tilde{T}) + \frac{\partial}{\partial x_j}(\bar{\rho}\tilde{u}_j\tilde{T}) = -\frac{\partial\overline{q_j}}{\partial x_j} - \frac{\partial Q_j}{\partial x_j} \tag{3}$$

where the filtered viscous stress tensor and heat conduction vector are given as,

$$\bar{\sigma}_{ij} = \overline{\frac{\mu}{Re}\left(\frac{\partial u_i}{\partial x_j} + \frac{\partial u_j}{\partial x_i} - \frac{2}{3}\frac{\partial u_k}{\partial x_k}\delta_{ij}\right)};$$
$$\bar{q}_j = \overline{\frac{k}{PrRe}\left(\frac{\partial T}{\partial x_j}\right)} \tag{4}$$

and the SGS stress tensor and heat conduction vector are given as,

$$\tau_{ij} = \bar{\rho}(\widetilde{u_i u_j} - \tilde{u}_i \tilde{u}_j); \quad Q_j = \bar{\rho}(\widetilde{u_j T} - \tilde{u}_j \tilde{T}) \tag{5}$$

The turbulent stress τ_{ij} and the turbulent heat flux Q_j have to be modeled in order to close the system of equations, and these terms represent the effect of the SGS velocity and temperature components on the evolution of the large scales. The Favre-filtered equation of state is $\bar{p} = \bar{\rho} R \tilde{T}$. Variations of viscosity and conductivity are given by the power-law form of Sutherland's formula (Schlichting, 1979)

$$\frac{\mu^*}{\mu_{\text{ref}}} = \left(\frac{T^*}{T_{\text{ref}}}\right)^{0.71}; \quad \frac{k^*}{k_{\text{ref}}} = \left(\frac{T^*}{T_{\text{ref}}}\right)^{0.71} \tag{6}$$

The Prandtl number Pr, and specific heat at constant pressure C_p, are treated as constants for the temperature range in consideration.

2.2. Sub-grid scale modeling

2.2.1. Smagorinsky model

The compressible flow version of the Smagorinsky model is given as

$$\tau_{ij} = \tfrac{1}{3}\tau_{kk}\delta_{ij} - 2\mu_{\text{T}}(\tilde{S}_{ij} - \tfrac{1}{3}\tilde{S}_{kk}\delta_{ij});$$
$$\tilde{S}_{ij} = \tfrac{1}{2}\left(\frac{\partial \tilde{u}_i}{\partial x_j} + \frac{\partial \tilde{u}_j}{\partial x_i}\right) \tag{7}$$

where μ_{T} is the eddy viscosity, and $\tilde{S}_{ij}$ is the Favre-filtered strain rate tensor. τ_{kk} is the SGS turbulent kinetic energy which needs to be modeled for the case of compressible flows. The model proposed by Yoshizawa (1986) can be written as

$$\tau_{kk} = 2C_I \bar{\rho} \Delta^2 |\tilde{S}|^2 \tag{8}$$

For closure, μ_{T} is parameterized by equating the SGS energy production and dissipation, and the SGS heat flux vector Q_j is modeled using a gradient-diffusion hypothesis as

$$\mu_{\text{T}} = C_{\text{s}} \bar{\rho} \Delta^2 \sqrt{2\tilde{S}_{ij}\tilde{S}_{ij}} \quad \text{and} \quad Q_j = -\frac{\bar{\rho} C_{\text{s}} \Delta^2 |\tilde{S}|}{Pr_{\text{T}}} \frac{\partial \tilde{T}}{\partial x_j} \tag{9}$$

where C_{s} is a model parameter to be specified and Pr_{T} is the turbulent Prandtl number defined as the ratio of eddy-viscosity ν_{T} to eddy-diffusivity α_{T}. Δ is the filter width which is typically assumed to be a function of the grid resolution, and calculated as $\Delta_{\text{av}} = (\Delta x \Delta y \Delta z)^{1/3}$.

2.2.2. Dynamic model procedure

The extension of the dynamic model for compressible flows proposed by Moin et al. (1991) has been used. The dynamic model procedure, in this study, employs the Smagorinsky model as its base model. The model parameter C_{s} and Pr_{T} are calculated "dynamically" using spectral information from two different levels already part of the resolved solution. The procedure requires the definition of a new "test" filtering operation where the test filter width $\hat{\Delta}$ is greater than the grid filter width, Δ (often by a ratio of 2, as was the case in this study). On application of the test filter to the filtered NS equations, one obtains the sub-test scale stress terms. The stresses at the two different filter levels are related by the algebraic identity of Germano (1992). A least-squares approach to error minimization (Lilly, 1992) enables the determination of C_{s} and Pr_{T}. Averaging along the spanwise direction was employed to prevent numerical instabilities in the determination of these model parameters. In addition the total viscosity and the total diffusivity were artificially set to zero at locations where the SGS model returned negative values.

3. Numerical procedure

A coupled finite volume procedure based on a collocated grid scheme was used to solve the filtered NS equations for the primitive variables [p, u, v, w, T]. The method was fully implicit, second order accurate in time, with advective terms discretized using second order central differences and viscous terms with fourth order central differences. Time derivative preconditioning (Pletcher and Chen, 1993) was incorporated to alleviate the stiffness and convergence problems associated with flows that occur with traditional compressible formulations at low-Mach numbers. An all-speed strategy has thus evolved that enables the application of the same methodology to incompressible flows and compressible flows at low-Mach numbers where effects of property variations need to be accounted for. A sixth order compact filter (Lele, 1992) was used to eliminate pressure–velocity decoupling peculiar to collocated-grid methods. The system of algebraic equations was solved using Stone's strongly implicit procedure (Stone, 1968; Weinstein et al., 1969). A code well optimized for performance on the CRAY T-90 was used to perform the large eddy simulations. Several aspects of the numerical procedure have been presented in detail by Wang (1995), Narayanan (1998) and Avancha (2001).

4. Problem description and simulation details

4.1. Geometry and flow conditions

The geometry of the domain of interest is shown in Fig. 1 and the fluid under consideration is air. The step height h was 0.041 m, and the upstream section had a height of 0.082 m (=$2h$), resulting in an expansion ratio of 1.5 (= $3h/2h$). The Reynolds number based on the step height and upstream centerline velocity was 5540. Reference values of some key physical parameters were:

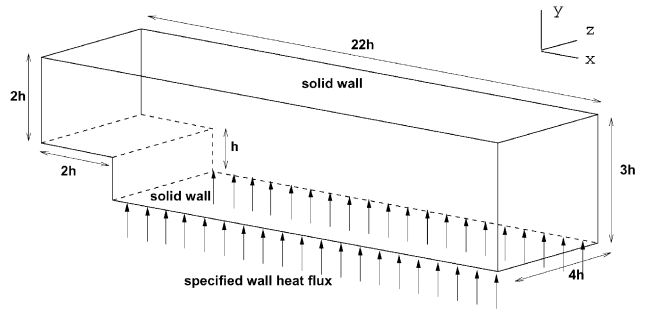

Fig. 1. Backward-facing step geometry.

$U = 2.063$ m/s, $T = 293.0$ K, $L = h = 0.041$ m, $\rho = 1.194$ kg/m^3, $k = 25.74 \times 10^{-3}$ W/m K, $v = 15.27 \times 10^{-6}$ m^2/s, $C_p = 1006.0$ J/kg K, and $Pr = 0.71$. These conditions were chosen so as to compare results from the isothermal flow simulations with the particle tracking velocimetry experiments of Kasagi and Matsunaga (1995), that are amongst the latest available results for this geometry. More importantly, the flow condition upstream of the step, and at separation was established as a fully developed turbulent channel flow. This was done by the experimentalists to ensure that no predictive calculations would suffer from incompleteness or ambiguity in the upstream boundary conditions. Many of the studies conducted, simulations and experiments alike, have a boundary layer of specific thickness at the point of separation, leaving open the issue of effect of the upstream condition on the mean reattachment length and the recirculation region. The state of the inflow condition has often been cited by the researchers as a potential source of disagreement with experimental data.

4.2. Grid resolution

The grid resolution used for the simulations was: (1) upstream of step: $17 \times 31 \times 48$, (2) downstream of step: $72 \times 46 \times 48$ in the streamwise, wall-normal and spanwise directions respectively. While the grid was uniform in the spanwise (z) direction, it was stretched in the streamwise (x) and wall-normal (y) directions using a hyperbolic tangent stretching scheme. The grid resolution for this study was arrived at after a careful consideration of the LES results of Akselvoll and Moin (1995) and conclusions from grid refinement studies conducted as a part of that study.

4.3. Boundary and initial conditions

No-slip boundary conditions were enforced at the top and bottom solid walls. Periodicity of flow was assumed in the spanwise direction. The NS characteristic boundary condition strategy (Poinsot and Lele, 1992) was employed at the inflow and outflow boundaries. Brief descriptions are provided in the following sections.

4.3.1. Inflow

Turbulent inflow conditions for each time step of the simulation were provided by planes of data stored from an independent LES of a channel flow with the same Reynolds number and time step. At the inlet, in order to enforce a constant mass flow rate, a constant density condition was used:

$$\bar{\rho} = \text{constant} \Rightarrow \frac{\bar{p}}{R\tilde{T}} = \text{constant} \tag{10}$$

Upon linearization of the above expression using a Newton linearization approach and written in the "delta" form (where the change in variables becoming the unknowns being solved for), one obtains

$$\frac{1}{R\tilde{T}}\Delta\bar{p} - \frac{\bar{p}}{R\tilde{T}^2}\Delta T = 0 \tag{11}$$

The above equation is solved for in an implicit fashion along with the other boundary conditions.

4.3.2. Outflow

In the case of subsonic flows, as was the case in this study, waves reflecting on regions far from the computational domain where some static pressure p_∞ is specified are responsible for conveying information from outside the domain to the interior. This information helps the flow determine the mean pressure. Partially non-reflecting boundary conditions as opposed to perfectly non-reflecting conditions are thus desirable. For subsonic flows, four characteristic waves with velocities $u_1 + c$, u, u, u leave the domain, while one characteristic wave enters the domain at a velocity of $u_1 - c$. The convective flux in the streamwise direction is represented in terms of the amplitude variations of these waves. The amplitude variations are expressed as a linear combination of the first derivatives of all the dependent variables with respect to the streamwise coordinate. The amplitude variation of the characteristic wave traveling upstream, $\mathscr{L}_1$, is specified by using the condition of constant pressure at infinity:

$$\mathscr{L}_1 = K(p - p_\infty); \quad K = \frac{\sigma(1 - M^2)c}{L} \tag{12}$$

where K is a constant used as a tuning parameter for the particular flow. If the outlet pressure is not close to p_∞, waves will enter the domain through the outlet to bring the mean pressure to a value close to p_∞. The larger the value of K, smaller the difference between the pressure at the outlet and p_∞. Values in the range of 0.25–5.0 for σ were chosen ensuring that the criterion of mass conservation was satisfied very well. By setting σ to zero, perfectly non-reflecting conditions can be obtained if needed. Amplitude variations corresponding to

outgoing waves ($\mathscr{L}_2$ through $\mathscr{L}_5$) can be computed from interior points using one-sided differences. In order to complete the outflow boundary condition, the streamwise derivatives of the shear stresses ($\partial\tau_{xy}/\partial x$, $\partial\tau_{xz}/\partial x$) and the heat flux vector $\partial q_x/\partial x$ are set to zero. The NS equations can then be advanced in time. For details regarding the NSCBC strategy, the reader is urged to refer to Poinsot and Lele (1992).

For the simulations with heat transfer, the bottom wall downstream of the step was the only one supplied with a uniform heat flux. The remaining walls were insulated (adiabatic conditions).

Prior to carrying out the simulations with heat transfer, an isothermal study was conducted. The geometry used for the isothermal simulations was retained with the hope that results from the LES would motivate new experimental work, in light of advances being made in measurement methods, to include the effects of heat transfer. Importantly, using the same geometry permits the use of the planes of channel flow data for inflow conditions, initial conditions for the heat transfer cases become easily available from the isothermal simulations, and result in significant savings in computer resources.

5. Results from isothermal flow simulation

The streamwise, wall-normal and spanwise mean velocity distributions, and the respective rms fluctuations from the simulation showed excellent agreement with experimental results of Kasagi and Matsunaga (1995). Third order moments also showed good qualitative agreement with the experiments. The mean reattachment length from the simulation was predicted to be $6.1x/h$, as compared with the $6.51x/h$ reported in the experiment. Details of the simulation and results have been presented in Avancha (2001) and Avancha and Pletcher (2000).

6. Results from constant wall heat flux simulations

For the simulations involving heat transfer, three different wall heat flux (q^*_w) levels of 1.0, 2.0, and 3.0 kW/m^2 corresponding to normalized heat flux, Q_w levels of 0.0014, 0.0028, 0.0042 were supplied to the surface downstream of the step. A Mach number of 0.006, and a non-dimensional physical time step of 0.03 were used. In the following sections results from these simulations will be presented and discussed. The effects of buoyancy for the range of heat flux levels used in this study were ascertained to be minimal, and therefore neglected.

6.1. Mean velocity and temperature distributions

Mean streamwise (Fig. 2), and wall-normal (Fig. 3) velocity profiles, from the simulations with heat transfer

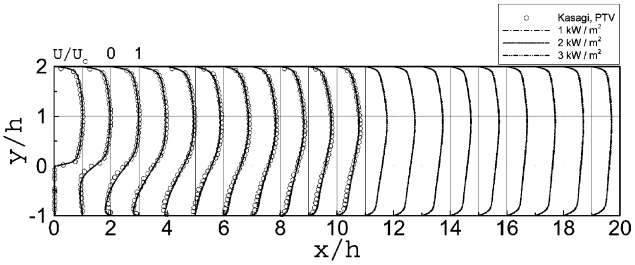

Fig. 2. Mean streamwise velocity.

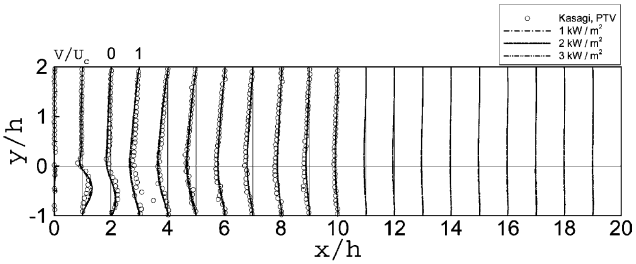

Fig. 3. Mean wall-normal velocity.

are in good agreement with the isothermal experimental results of Kasagi and Matsunaga (1995). The mean streamwise velocity profiles demonstrate the growth of the shear layer by entrainment of fluid, and its subsequent contact with the wall at the reattachment point. The reattachment point is defined as the length between from the step face to the point of zero mean skin friction and the reattachment point is not fixed but oscillates over a distance of ± 1 step height (Fig. 4). Eaton and Johnston (1980) found that the "flapping" of the shear layer normal to the wall causes its impingement point to move slowly back and forth over a range of ± 1 step height. The mean wall-normal velocity profiles, downstream of $x/h \sim 2$, are negative, implying that the shear layer is bending toward the wall. Downstream of reattachment, the mean wall-normal velocity is small and indicates the development of a wall-bounded flow. Integration of the streamwise mass flow across the channel height shows that the mass flow rate variations are within 2%, and that the conservation of mass is satisfied very well. The presence of a counter-rotating corner

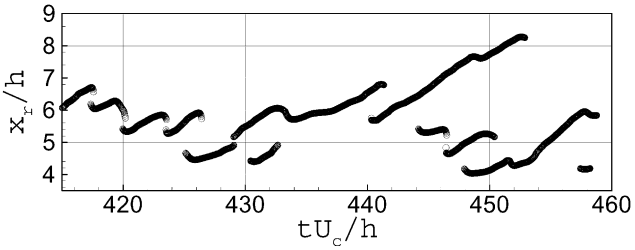

Fig. 4. Temporal variation of the spanwise average reattachment locations.

eddy has been captured (Fig. 5), and is important in the predicted heat transfer rate close to the step.

Significant gradients in the spanwise- and time-averaged temperature, $\langle T\rangle_{zt}$ (Fig. 6) are confined to the near-wall region along the length of the downstream section; most of the temperature drop appears to occur within a fraction of the step height from the bottom wall. Expanded near-wall region plots of $\langle T\rangle_{zt}$ profiles at different streamwise stations are shown in Figs. 7 and 8. The only region away from the wall where significant mean temperature gradients are observed is immediately downstream of the step. These gradients can be attributed to the activity of the counter-rotating corner eddy as well as the larger recirculation eddy that are responsible for pushing up (as evidenced by the positive wall-normal velocity profiles near the step up to $x/h \sim 2$) warm packets of fluid while simultaneously relatively "colder" packets of fluid are introduced into the same region by the shear layer. It was confirmed from animations of the instantaneous temperature, that convective mixing effects prohibit significant temperature gradients in other regions of the flow. Downstream of reattachment, the growth of the thermal boundary layer is clearly discernible from examining the spread of the mean temperature gradients in Figs. 7 and 8.

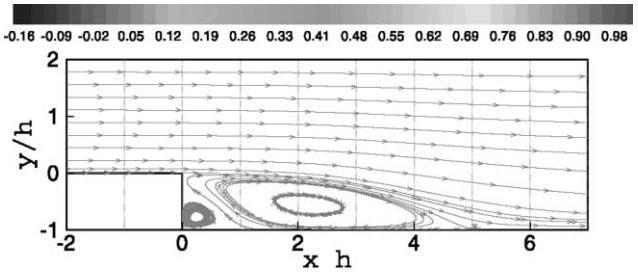

Fig. 5. Mean streamlines.

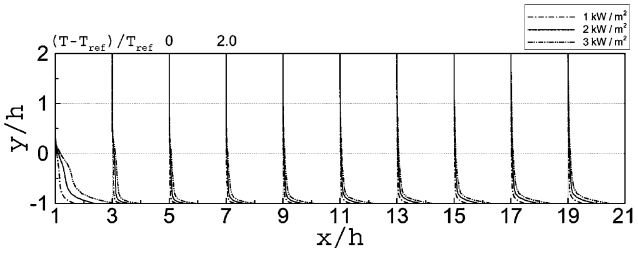

Fig. 6. Mean temperature.

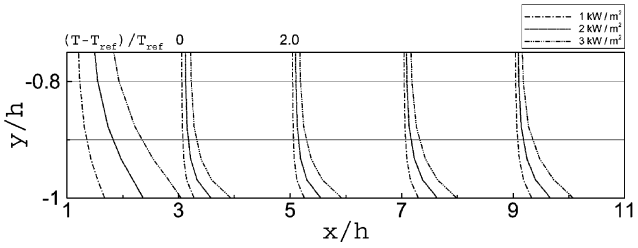

Fig. 7. Mean temperature (expanded plot).

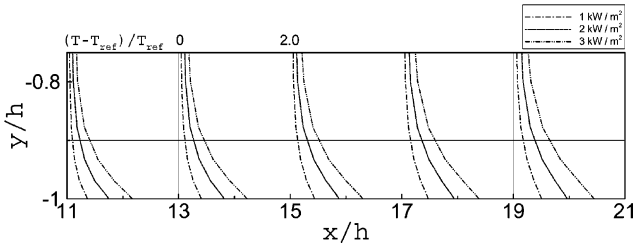

Fig. 8. Mean temperature (expanded plot).

The heat flux levels of 1.0, 2.0, 3.0 kW/m^2 yield maximum $\langle T_{\text{wall}}\rangle_{zt}/\langle T_{\text{bulk}}\rangle_{zt}$ ratios of about 1.7, 2.3, and 2.9 respectively, where the bulk temperature is given by:

$$T_{\text{bulk}} = \frac{\int_y \int_z \rho u C_p T \,\mathrm{d}y\,\mathrm{d}z}{\int_y \int_z \rho u C_p \,\mathrm{d}y\,\mathrm{d}z} \tag{13}$$

The bulk temperature profiles (Fig. 9) are in good agreement with analytical estimates based on an overall energy balance for the uniform heat flux condition. The wall temperatures (Fig. 10) show a dramatic increase downstream of the step, reaching their peak values in the neighborhood of the streamwise distance of $x/h \sim 2$. This increase in wall temperature is accompanied by a decrease in convective heat transfer (as evidenced by the Stanton number profiles in Fig. 11), and suggests that the air in this zone is almost in a "stagnant" state. In the neighborhood of $x/h \sim 0.5$, St attains its minimum value for the three different heat flux cases—suggesting that the dominant mode of heat transfer in this region, close to the step face, is through conduction. The relatively thicker viscous sub-layer close to the step, that can

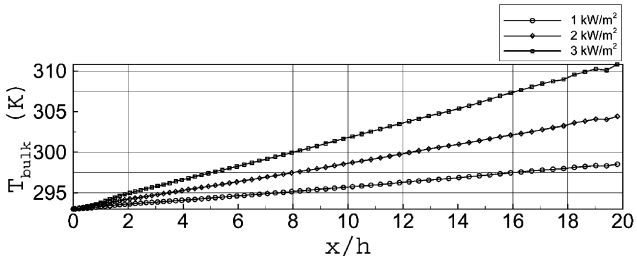

Fig. 9. Bulk temperature.

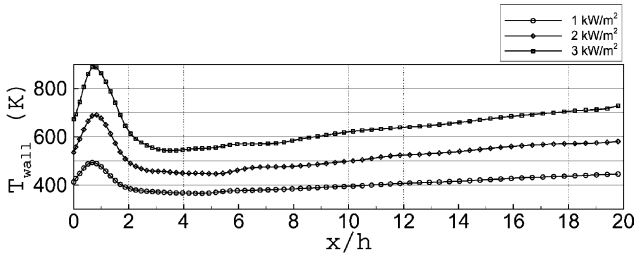

Fig. 10. Wall temperature.

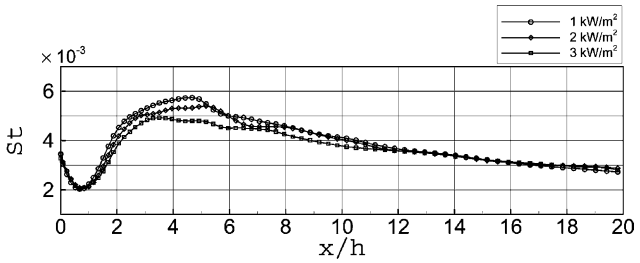

Fig. 11. Mean Stanton number.

be inferred from inspection of the mean temperature profiles in wall coordinates, provides evidence to support this suggestion. Away from the step face, the wall temperature profiles drop significantly, accompanied by a steep rise in the Stanton number profiles that suggest increased heat transfer due to convection. The Stanton number profiles attain a maximum slightly upstream of reattachment, which is in agreement with Vogel and Eaton (1984), as opposed to several other studies that have assumed the location of the peak Stanton (or Nusselt) number to coincide with the mean reattachment point.

Farther downstream, in the region of reattachment, the impinging shear layer is responsible for the depression in the wall temperature around reattachment. A linear increase of the wall temperatures downstream of reattachment and a monotonic decrease in the mean Stanton number profiles is consistent with the growth of the thermal boundary layer following reattachment.

Profiles of the mean streamwise velocity and temperature (Figs. 12 and 13) in wall coordinates have been plotted for various streamwise stations, starting from immediately downstream of the step and continuing to the exit station. The linear law, $u^+ = y^+$ and the log-law, $u^+ = 2.5 \ln y^+ + 5.5$ for the velocity and the thermal linear law, $T^+ = Pry^+$ and the thermal log-law $T^+ = 2.78 \ln y^+ + 2.09$ are also shown on the plots. Profiles of mean streamwise velocity and temperature (Figs. 14 and 15) in semi-local coordinates have also been plotted, and the temperature profiles showed a tendency to collapse for the different heat flux cases beyond the viscous sub-layer downstream of reattachment (Avancha, 2001). Clearly, the 'law of the wall' and its thermal counter-part do not hold within the recirculating region.

Downstream of reattachment, as the velocity and thermal boundary layers develop, the mean profiles tend towards the 'law of the wall' but complete agreement can only be expected when the downstream flow reaches a fully developed state for the velocity and temperature. From a study of the mean velocity and temperature profiles plotted in the wall and semi-local coordinates it becomes clear that the viscous sub-layer is responsible for most of the thermal resistance in the flow. Where the viscous sub-layer is thick (estimated by a visual

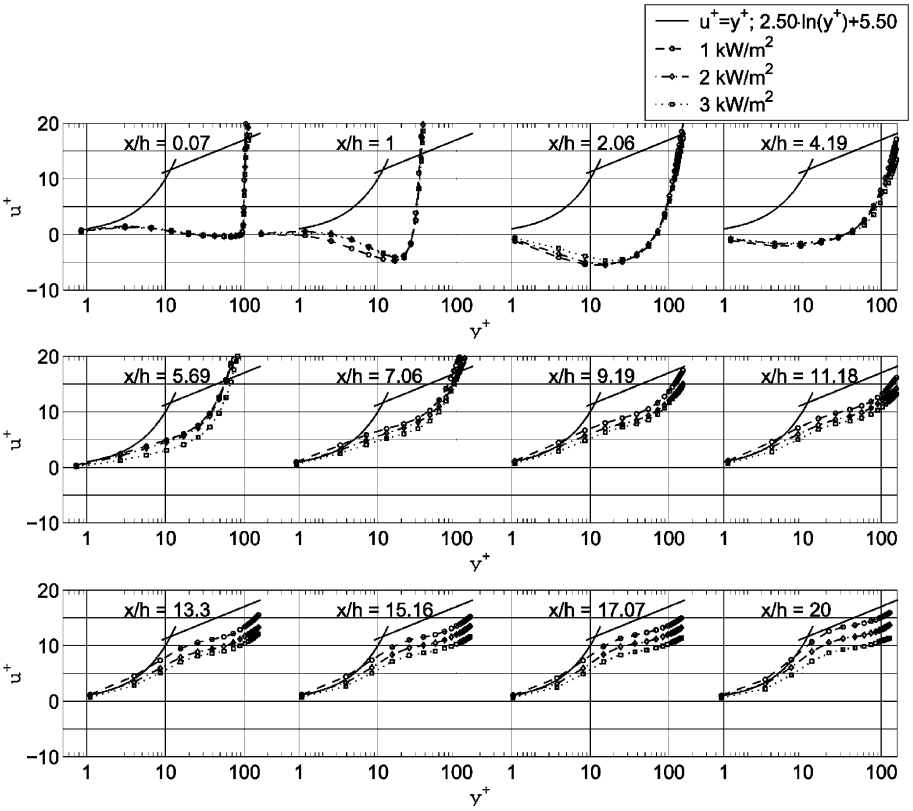

Fig. 12. Mean streamwise velocity in wall coordinates.

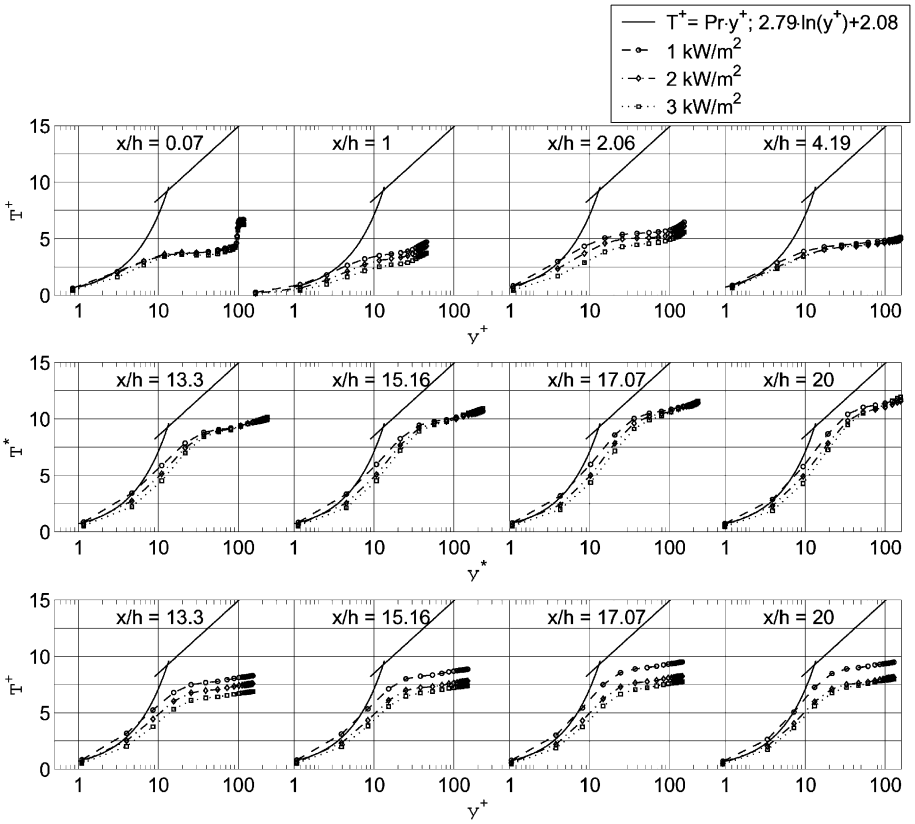

Fig. 13. Mean temperature in wall coordinates.

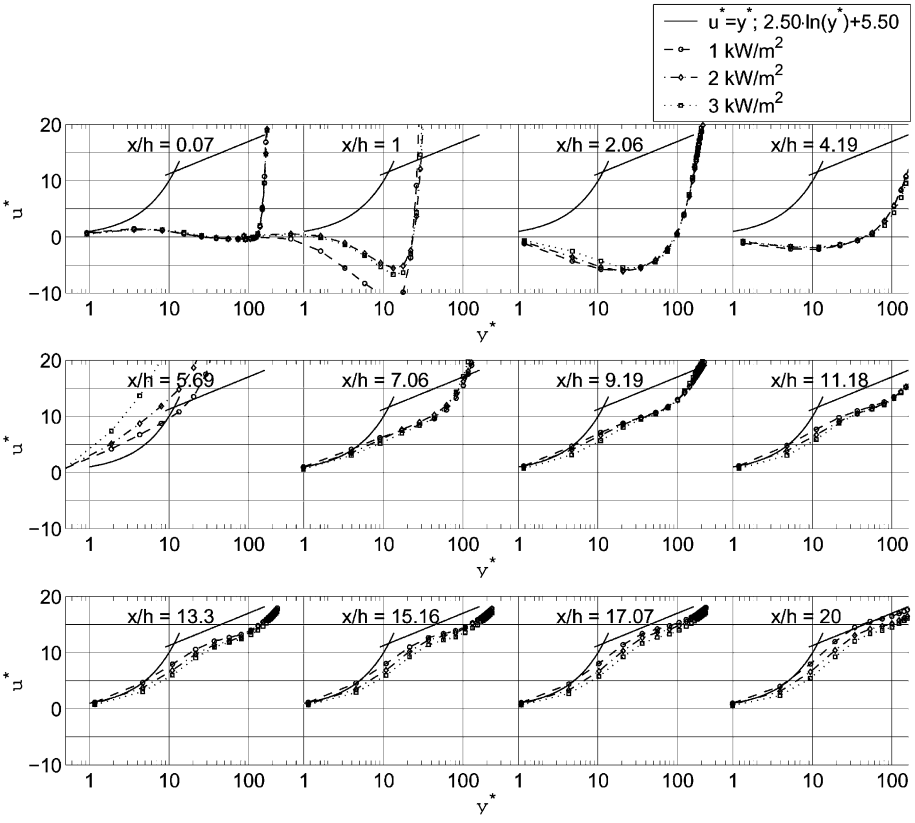

Fig. 14. Mean streamwise velocity in semi-local coordinates.

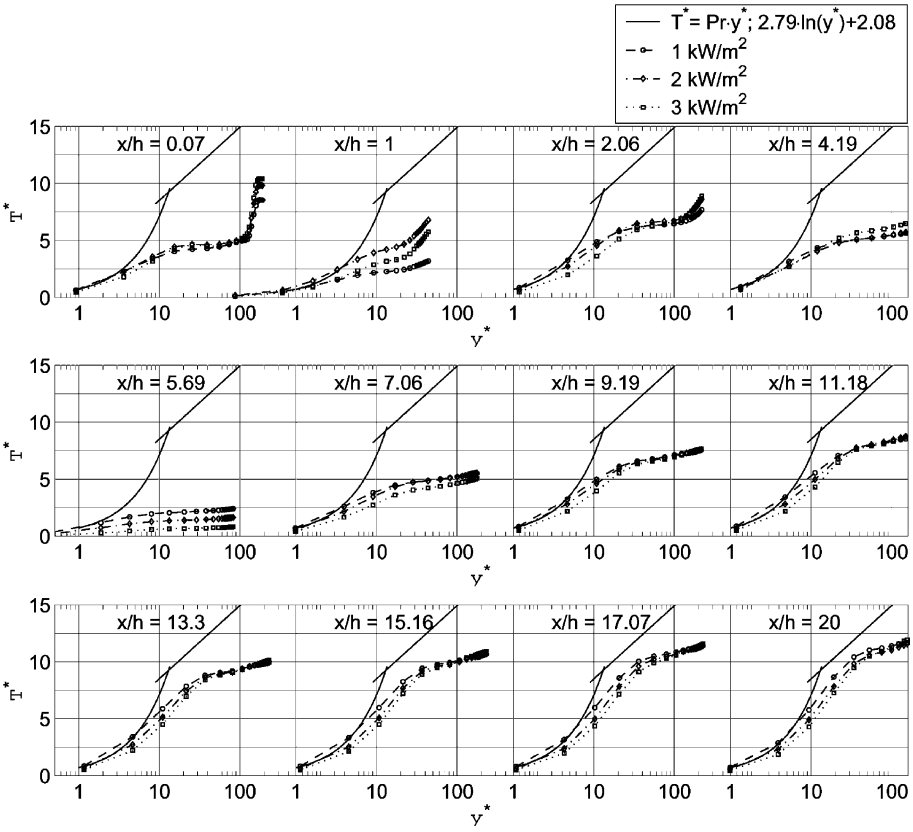

Fig. 15. Mean temperature in semi-local coordinates.

examination of the plots, as to the first point of departure from the $y^+ = u^+$, or $y^+ = T^+$ curves), the Stanton number falls. Correspondingly, where the viscous sub-layer is at its thinnest, the Stanton number is at its peak value. The Stanton number takes on a minimum close to the step at about $x/h = 1.0$; and one-to-one correspondence between this behavior of the Stanton number and the thickness of the viscous sub-layer can be made from observation of the mean temperature profiles in wall coordinates at the streamwise stations of $x/h = 0.07$ until the streamwise station of $x/h = 1.0$. This correspondence can be observed by continuing to track these profiles at the subsequent streamwise stations, where a thickening of the viscous sub-layer takes place until the streamwise station of $x/h = 3.07$, beyond which the viscous sub-layer again demonstrates a pattern of thinning until the streamwise station of $x/h = 6.22$. No further thinning of the viscous sub-layer can be observed at stations beyond $x/h = 6.22$, and this is in keeping with the growth of the thermal boundary layer.

6.2. Reynolds analogy?

From inspection of the Stanton number profiles (Fig. 11) and the mean skin-friction profiles (Fig. 16) we can conclude that the Reynolds analogy,

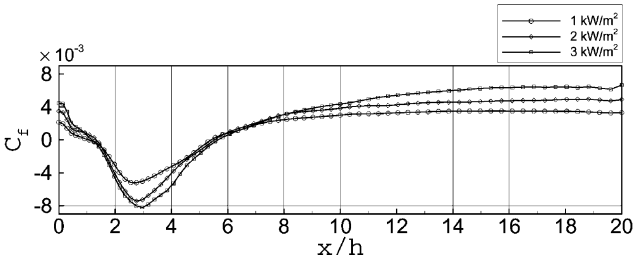

Fig. 16. Mean skin-friction coefficient.

$$St = \frac{C_f}{2} \tag{14}$$

does not hold in the recirculating region of the flow. Close to the step, both the Stanton number and skin-friction coefficient are small in magnitude and show a downward trend; the Stanton number attains its minimum close to the step and this implies a low level of convective heat transfer in this region. It is at these points of minimum Stanton number that the wall temperature (Fig. 10) takes on the maximum values. Rapid change in both St and C_f is observed in recirculating region. The skin-friction coefficient drops by three times the value at the step for the 3.0 kW/m^2 case, before starting to rise to zero at reattachment; the Stanton

number rises from its minimum close to the step and attains a peak value upstream of reattachment suggesting a gradual increase in heat transfer due to convective mixing. Downstream of reattachment the two profiles start to resemble their flat-plate boundary layer counterparts.

While the Reynolds analogy does not hold in the mean sense in the recirculation region, it is possible that it might hold in an instantaneous sense. For this to be true, one would expect the mean Stanton number to be correlated with the time average of the absolute value of the skin-friction coefficient (Vogel and Eaton, 1984). Comparing Figs. 11 and 17, it is seen that close to the step, the absolute value of the skin-friction coefficient and the Stanton number show downward trends and start to climb at nearly the same streamwise location.

At roughly $x/h \sim 3.0$, the absolute value of the skin-friction coefficient and Stanton number diverge strongly from each other, nevertheless maintaining their positive values. It is in this sense of measure of sign, that the Stanton number agrees better with the absolute value of the skin-friction coefficient than it does with the mean skin-friction coefficient.

However, it is very interesting to note that the mean Stanton number profiles (Fig. 11) show a more striking similarity with the fluctuating skin-friction coefficient profiles (Fig. 18),than they do with the average absolute skin-friction coefficient (Fig. 17). The fluctuating skin-friction coefficient is computed as:

$$C_f' = \sqrt{\left(\langle C_f \rangle_z - C_f\right)^2} \tag{15}$$

and subsequently a span- and time-averaged value $\langle C_f' \rangle_{zt}$ is computed. The Stanton number profiles and the skin-friction coefficient show a downward trend close to the step, before the subsequent peak values upstream of reattachment. At reattachment itself, however, both the profiles start to relax from the peak values. Vogel and Eaton (1984) indicate that this strong correlation between the fluctuating skin-friction coefficient and the Stanton number suggests that the correct velocity scale governing the strength of convective effects in the reattachment zone must be related to the velocity fluctuations rather than the mean velocity.

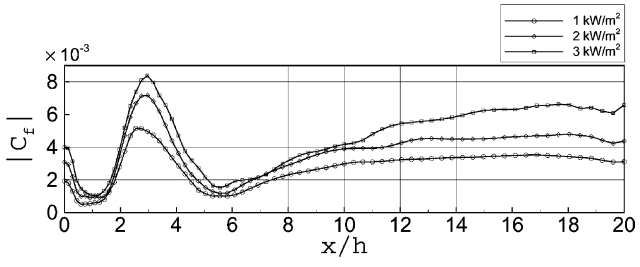

Fig. 17. Average of absolute skin-friction coefficient.

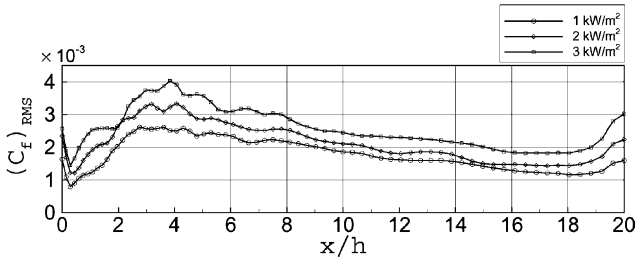

Fig. 18. Fluctuating skin friction.

6.3. Velocity and temperature fluctuations

The rms velocity fluctuations from the simulations with the different wall heat fluxes show excellent agreement with the experimental results. It must be recalled that there is no heat transfer involved in the experiments.

The level of temperature fluctuations depends on the local length scales of velocity and temperature. If the temperature gradient is small, then large velocity fluctuations are necessary to create large temperature fluctuations. If the temperature gradient is large, then even small velocity fluctuations can result in large temperature fluctuations. The rms temperature fluctuations are shown in Fig. 19. The highest level of temperature fluctuations is close to the step face, downstream of separation. The magnitude of the fluctuations across the shear layer decreases downstream of separation. These fluctuations in temperature are a result of "warm" fluid being transported upwards away from the wall, as evidenced by the positive wall-normal velocity, being exposed to "cooler" fluid being entrained into the same region by the separating shear layer. A gradual decrease of the temperature fluctuations away from the bottom wall can be observed, although we can observe an increase in the depth of penetration of these fluctuations. The peak levels in the temperature fluctuations, however, remain confined to the near-wall region for all streamwise stations. It is also obvious that the temperature fluctuations show an increase in magnitude with increasing values of wall heat flux.

The higher mean temperature gradients coupled with the velocity fluctuations result in large temperature fluctuations close to the step face. Farther downstream, the mean temperature gradients are confined to the

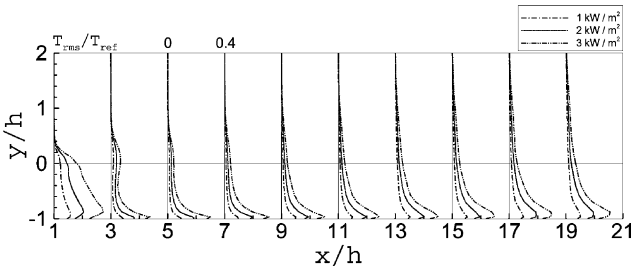

Fig. 19. Rms temperature fluctuations.

near-wall region and with a concentration of velocity fluctuations close to the wall, the temperature fluctuations are greatest near the wall. Downstream of reattachment, the mean temperature gradients show a greater spread away from the wall, and the fluctuations in temperature follow this spread. Essentially, the velocity fluctuations play an important role in giving rise to fluctuations in temperature.

6.4. Cross-correlations of the velocity and temperature fluctuations

The cross-correlations of the velocity and temperature fluctuations $\langle \rho u'' T'' \rangle_{zt}$, $\langle \rho v'' T'' \rangle_{zt}$, shown in Figs. 20 and 21, represent the streamwise and wall-normal turbulent heat flux components based on Favre-averaged fluctuations. The transport of energy across the shear layer immediately downstream of the step is through the wall-normal turbulent heat flux, $\langle \rho v'' T'' \rangle_{zt}$. It drops sharply on the warmer side of the shear layer (possibly indicating that the transport of energy here is by a mechanism other than the wall-normal velocity fluctuations) before it increases in the near-wall region (where the temperature fluctuations are larger than elsewhere owing to the large temperature gradients in combination with all components of velocity fluctuations). It is interesting to note that, at this same streamwise station, the streamwise turbulent heat flux $\langle \rho u'' T'' \rangle_{zt}$ shows a positive peak in the near-wall region and negative peak on the warmer side of the shear layer. The behavior of the streamwise turbulent heat flux, close to the step face, is a result of the non-negligible gradients of temperature and streamwise velocity fluctuations. The temperature gradients in streamwise direction are most likely due to the interplay between "colder" packets of fluid being entrained by the shear layer at separation and the "warmer" packets of fluid traveling upstream within the recirculation bubble. Farther downstream, a decrease in the vertical turbulent heat flux is observed, going away from the wall. However, as the thermal boundary layer develops and grows, the turbulence levels are higher, and the magnitude of the vertical and streamwise turbulent heat fluxes successively increase downstream. The depth to which these turbulent fluxes penetrate also increases downstream.

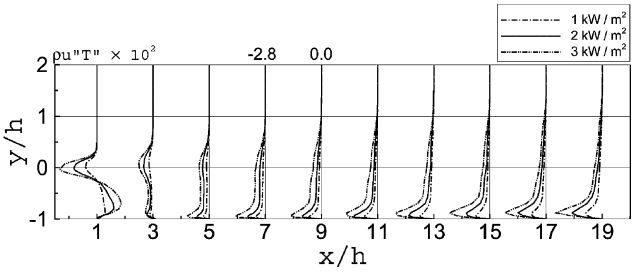

Fig. 20. Streamwise turbulent heat flux.

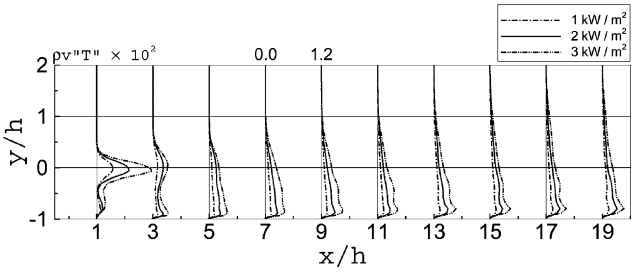

Fig. 21. Vertical turbulent heat flux.

From their experiments Vogel and Eaton (1984) concluded that the streamwise turbulent heat flux was negligible as compared to the wall-normal turbulent heat flux. However, we show that the streamwise turbulent heat flux (Fig. 20) and the wall-normal turbulent heat flux (Fig. 21) are of the same order of magnitude. The heat flux levels, and consequently the temperature gradients, in this work are an order of magnitude greater than in their study, and the Reynolds numbers are three to five times smaller. These are probable reasons for their observation of negligible streamwise turbulent heat flux in comparison with the vertical turbulent heat flux. The turbulent Prandtl number (Fig. 22), as computed

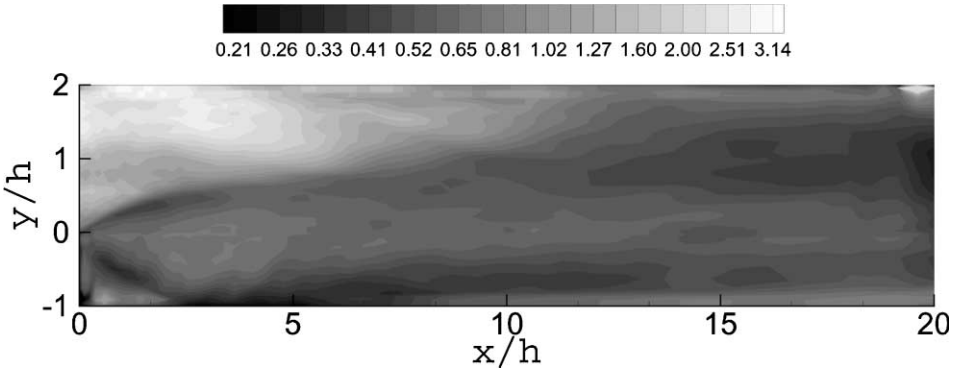

Fig. 22. Turbulent Prandtl number (computed from the dynamic model).

from the dynamic SGS model shows a strong spatial variation, especially in the region close to the step. This strong spatial variation suggests that the use of a constant turbulent Prandtl number in the modeling of turbulent heat fluxes adopted in many RANS approaches might not be accurate. The spanwise turbulent heat flux was also computed and no specific conclusions could be drawn other than the fact that the transport of energy was much smaller through this mode of transport.

6.5. Density fluctuations and property variations

Rms density fluctuations, expressed as a percentage of the local span- and time-averaged density ρ_{av}, of up to 20% are observed in Fig. 23. Density fluctuations can largely be attributed to the large density gradients in the flow (approximately inversely proportional to the temperature gradients) and velocity fluctuations.

At the peak wall temperatures for the three heat flux cases, the viscosity and thermal conductivity are roughly about 20%, 40% and 60% greater than the values at the inlet, which are at the reference temperature of 293 K, thus demonstrating the need for property variations to be considered in calculations involving high heat fluxes. For example, the skin-friction coefficient and friction velocity show a functional dependence on the thermal conductivity k, and dynamic viscosity μ. The variation in these two properties due to temperature is shown in Figs. 24 and 25. Substantial change in the computed values of skin friction, as in Fig. 16, is observed for the variations in dynamic viscosity, especially for the range of wall temperatures encountered in this study. All the calculations included in the review by Abrous and Emery (1996) have used wall heat flux values of 5.0 kW/m^2 and relied on the assumption of constant properties, and it is our contention that it is important to consider the effects of property variations.

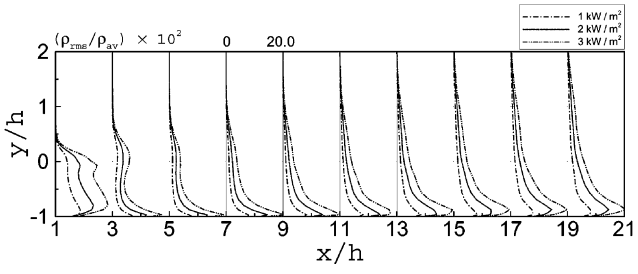

Fig. 23. Rms density fluctuations.

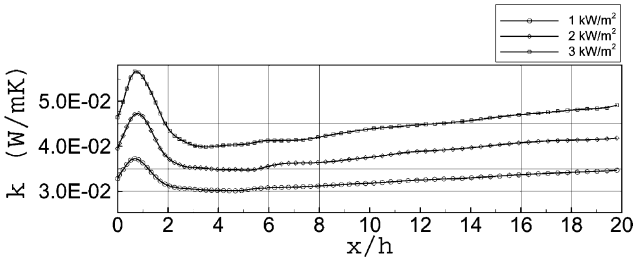

Fig. 24. Variation in thermal conductivity.

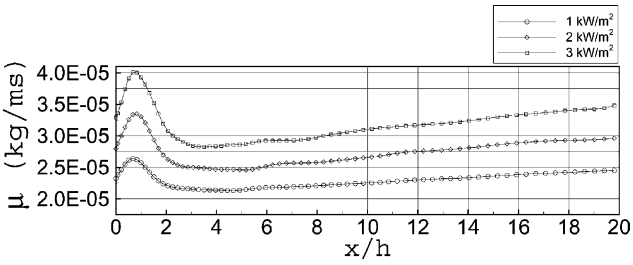

Fig. 25. Variation in dynamic viscosity.

7. Conclusions

Large eddy simulations to study the heat transfer and fluid dynamics of the turbulent reattaching flow past a backward-facing step have been successfully conducted. The choice of the formulation enabled the inclusion of property variations, and facilitated the study at low-Mach numbers. Bulk temperature profiles are in excellent agreement with analytical estimates. Dramatic variation of the wall temperatures in the recirculation region is observed with a steep increase in wall temperature close to the step accompanied by a decrease in convective heat transfer. The peak heat transfer rate occurs slightly upstream of reattachment. The viscous sub-layer plays a critical role controlling the rate of heat transfer, and a strong correlation between the Stanton number and the thickness of the viscous sub-layer has been shown. The Reynolds analogy for the mean flow is not valid for a flow with separation and reattachment, certainly not within the recirculation region. However, the Stanton number profiles show a striking similarity with the fluctuating skin-friction coefficient profiles. Streamwise and wall-normal turbulent heat fluxes, indicative of thermal energy transport due to turbulence, are of the same order of magnitude. For the range of wall temperatures encountered, rms density fluctuations of up to 20% are observed, as are significant variations in viscosity and thermal conductivity.

Acknowledgements

The current research was partially supported by the Air Force Office of Scientific Research under grant F49620-94-1-0168 and by the National Science Foundation under grants CTS-9414052 and CTS-9806989. The use of computer resources provided by the National Partnership for Advanced Computational Infrastructure

at the San Diego Supercomputing Center is gratefully acknowledged.

References

Abe, K., Kondoh, T., Nagano, Y., 1994. A new turbulence model for predicting fluid flow and heat transfer in separating and reattaching flows: I. Flow field calculations. Int. J. Heat Mass Transf. 37 (1), 137–151.

Abe, K., Kondoh, T., Nagano, Y., 1995. A new turbulence model for predicting fluid flow and heat transfer in separating and reattaching flows: II. Thermal field calculations. Int. J. Heat Mass Transf. 38 (8), 1467–1481.

Abrous, A., Emery, A.F., 1996. Benchmark computational results for turbulent backward facing step flow with heat transfer. In: National Heat Transfer Conference. Vol. 9 of Heat Transfer Division, Vol. 331. ASME.

Akselvoll, K., Moin, P., 1995. Large eddy simulation of turbulent confined coannular jets and turbulent flow over a backward facing step. Report TF-63, Department of Mechanical Engineering, Stanford University.

Arnal, M., Friedrich, R., 1991. On the effects of spatial resolution and subgrid-scale modeling in large eddy simulation of a recirculating flow. In: Proceedings of the Ninth GAMM Conference on Numerical Methods in Fluid Mechanics.

Arnal, M., Friedrich, R., 1992. Large eddy simulation of a turbulent flow with separation. In: Turbulent Shear Flows, Vol. 8. Elsevier Science, pp. 169–187.

Avancha, R.V.R., 2001. A study of the heat transfer and fluid mechanics of the turbulent separating and reattaching flow past a backward facing step using large eddy simulation. Ph.D. Thesis, Iowa State University.

Avancha, R.V.R., Pletcher, R.H., 2000. Large eddy simulation of the turbulent flow past a backward facing step. AIAA Paper (2000-0542).

Ciofalo, M., Collins, M.W., 1989. k–ϵ predictions of heat transfer in turbulent recirculating flows using an improved wall treatment. Numer. Heat Transf. B 15, 21–47.

Eaton, J.K., Johnston, J.P., 1980. Turbulent flow reattachment: An experimental study of the flow and structure behind a backward facing step. Report MD-39, Thermosciences Division, Department of Mechanical Engineering, Stanford University.

Friedrich, R., Arnal, M., 1990. Analysing turbulent backward facing step flow with the lowpass-filtered Navier–Stokes equations. J. Wind. Engng. Indust. Aerod. 35, 101–128.

Germano, M., 1992. Turbulence: The filtering approach. J. Fluid Mech. 238, 325–336.

Kasagi, N., Matsunaga, A., 1995. Three-dimensional particle-tracking velocimetry measurement of turbulence statistics and energy budget in a backward facing step flow. Int. J. Heat Fluid Flow 16, 477–485.

Lele, S.K., 1992. Compact finite difference schemes with spectral-like resolution. J. Comput. Phys. 103, 16–42.

Lilly, D.K., 1992. A proposed modification of the Germano subgrid-scale closure method. Phys. Fluids A 4, 633–635.

Meakin, R.L., Street, R.L., 1988. Simulation of environmental flow problems in geometrically complex domains. Comput. Meth. Appl. Mech. 68, 151–175.

Moin, P., Squires, K., Cabot, W., Lee, S., 1991. A dynamic subgrid-scale model for compressible turbulence and scalar transport. Phys. Fluids A 3, 2746–2757.

Mori, Y., Uchida, Y., Sakai, K., 1986. A study of the time and spatial structure of heat transfer performances near the reattaching point of separated flows. In: Proceedings of the Eighth International Heat Transfer Conference, pp. 1083–1088.

Morinishi, Y., Kobayashi, T., 1990. Large eddy simulation of backward facing step flow. In: Rodi, W., Martelli, M. (Eds.), Engineering Turbulence Modeling and Experiments. Elsevier Science, Amsterdam.

Nagano, Y., Shimada, M., 1996. Development of a two-equation heat transfer model based on direct simulations of turbulent flows with different Prandtl numbers. Phys. Fluids A 8 (12), 3379–3402.

Narayanan, C., 1998. Colocated-grid finite volume formulation for the large eddy simulation of incompressible and compressible turbulent flows. Master's thesis, Iowa State University.

Neto, A.S., Grand, D., Mètais, O., Lesieur, M., 1993. A numerical investigation of coherent vortices in turbulence behind a backward facing step. J. Fluid Mech. 256, 1–25.

Pletcher, R.H., Chen, K.H., 1993. On solving the compressible Navier–Stokes equations for unsteady flows at very low-Mach numbers. AIAA Paper (93-3368).

Poinsot, T.J., Lele, S.K., 1992. Boundary conditions for direct simulations of compressible viscous flows. J. Comput. Phys. 101, 104–129.

Rosenfeld, M., Kwak, D., Vinokur, M., 1991. A fractional step solution method for the unsteady incompressible Navier–Stokes equations in generalized coordinate systems. J. Comput. Phys. 94, 102–137.

Schlichting, H., 1979. Boundary Layer Theory, second ed. McGraw-Hill, New York.

Shyy, W., Vu, T.C., 1991. On the adoption of velocity variable and grid system for fluid flow computation in curvilinear coordinates. J. Comput. Phys. 92, 82–105.

Stone, H.L., 1968. Iterative solution of implicit approximations of multidimensional partial differential equations. SIAM J. Numer. Anal. 5, 531–558.

Vogel, J.C., Eaton, J.K., 1984. Heat transfer and fluid mechanics measurements in the turbulent reattaching flow behind a backward facing step. Report MD-44, Thermosciences Division, Department of Mechanical Engineering, Stanford University.

Wang, W.-P., 1995. Coupled compressible and incompressible finite volume formulation for the large eddy simulation of turbulent flow with and without heat transfer. Ph.D. Thesis, Iowa State University.

Weinstein, H.G., Stone, H.L., Kwan, T.V., 1969. Iterative procedure for solution of systems of parabolic and elliptic equations in three dimensions. Ind. Eng. Chem. Fund. 8, 281–287.

Yoshizawa, A., 1986. Statistical theory for compressible turbulent shear flows, with the application to subgrid modeling. Phys. Fluids A 5, 3186–3196.

Zang, Y., Street, R.L., Koseff, J.R., 1991. In: Taylor, C. et al. (Eds.), Proceedings of the Seventh International Conference on Numerical Methods in Laminar and Turbulent Flow.

Zang, Y., Street, R.L., Koseff, J.R., 1994. A non-staggered grid, fractional step method for time-dependent incompressible Navier–Stokes equations in curvilinear coordinates. J. Comput. Phys. 114, 18–33.